Journal of Nuclear Science and Technology

ISSN: 0022-3131 (Print) 1881-1248 (Online) Journal homepage: http://www.tandfonline.com/loi/tnst20

3D Simulation of Solid-Melt Mixture Flow with Melt Solidification Using a Finite Volume Particle Method

Rida SN MAHMUDAH , Masahiro KUMABE , Takahito SUZUKI , Liancheng GUO & Koji MORITA

To cite this article: Rida SN MAHMUDAH , Masahiro KUMABE , Takahito SUZUKI , Liancheng GUO & Koji MORITA (2011) 3D Simulation of Solid-Melt Mixture Flow with Melt Solidification Using a Finite Volume Particle Method, Journal of Nuclear Science and Technology, 48:10, 1300-1312

To link to this article: http://dx.doi.org/10.1080/18811248.2011.9711820

Published online: 05 Jan 2012.

Journal of NUCLEAR SCIENCE and TECHNOLOGY, Vol. 48, No. 10, p. 1300–1312 (2011)

ARTICLE

3D Simulation of Solid-Melt Mixture Flow with Melt Solidification Using a Finite Volume Particle Method

Rida SN MAHMUDAH*, Masahiro KUMABE, Takahito SUZUKI, Liancheng GUO and Koji MORITA

Department of Applied Quantum Physics and Nuclear Engineering, Kyushu University, 744 Motooka, Nishi-ku, Fukuoka 8190395, Japan

(Received January 7, 2011 and accepted in revised form May 23, 2011)

Relocation and freezing of molten core materials mixed with solid phases are among the important thermal-hydraulic phenomena in core disruptive accidents of a liquid-metal-cooled reactor (LMR). To simulate such behavior of molten metal mixed with solid particles flowing onto cold structures, a computational framework was investigated using two moving particle methods, namely, the finite volume particle (FVP) method and the distinct element method (DEM). In FVP, the fluid movement and phase changes are modeled through neighboring fluid particle interactions. For mixed-flow calculations, FVP was coupled with DEM to represent interactions between solid particles and between solid particles and the wall. A 3D computer code developed for solid-liquid mixture flows was validated by a series of pure- and mixed-melt freezing experiments using a low-melting-point alloy. A comparison between the results of experiments and simulations demonstrates that the present computational framework based on FVP and DEM is applicable to numerical simulations of solid-liquid mixture flows with freezing process under solid particle influences.

KEYWORDS: moving particle methods, finite volume particle (FVP) method, distinct element method (DEM), multiphase flow with phase change

I. Introduction

A reasonable evaluation of relocation and freezing of molten core materials mixed with various solid phases is of importance in the safety analysis of liquid-metal-cooled reactors (LMRs). In core disruptive accidents (CDAs) of an LMR, there is the hypothetical possibility of whole-core disassembly due to overheating caused by a serious transient overpower and transient undercooling accidents. These will lead to the formation of a multicomponent, multiphase flow due to the existence of a mixture of molten fuel, molten steel, fission gas, coolant vapor, refrozen fuel, broken fuel pellets, and other structural materials. The solid fuel particles, which originate from early fuel pellet disruption and/or refreezing of molten fuel, could mix with the molten cladding material and start to flow through coolant flow channels. This is one of the important issues in blockage formation in the channels.

Many studies on liquid metal freezing have been conducted to understand the thermal-hydraulic phenomena in CDA of LMRs. Typical experimental studies are concerned with, for example, molten jet-coolant interactions by Kondo *et al.*,[1] thermite melt injection into an annular channel by Peppler *et al.*,[2] and molten-metal penetration and freezing behavior by Rahman *et al.*[3] and Hossain *et al.*[4] In the latter two studies,[3,4] numerical simulations were also performed using a 2D Eulerian reactor safety analysis code, SIMMER-III.[5,6] Although their simulations show reasonably good agreement with observed experimental results, in general, Eulerian methods are limited in reproducing local freezing processes in detail because such methods cannot capture phase changes at the interface. In addition, the particular shape of flowing molten metal cannot be represented by mesh methods. The present study is therefore aimed at developing a reasonable computational framework that can simulate the freezing and penetration behavior of molten metal and solid mixture flows onto a metal structure.

Conventional Eulerian methods encounter difficulties in representing complex flow geometries and to directly simulate the flow regime of mixed flows. Lagrangian methods represent one possible approach to overcome these problems. Several moving particle methods, which are fully Lagrangian methods, have been developed in recent years. The earliest of these is the smoothed particle hydrodynamics (SPH) by Monaghan,[7] which was specifically developed for compressible fluid calculations in astrophysics. The others are the moving particle semi-implicit (MPS) method[8] and the finite volume particle (FVP) method,[9] which can be applied to incompressible multiphase flows in complex geometries. It has been validated that these are able to simulate multiphase-flow behavior with satisfactory results,

*Corresponding author, E-mail: rida@nucl.kyushu-u.ac.jp

such as fragmentation of molten metal in vapor explosions,[10] water dam breakage with solid particles,[11] and a rising bubble in a stagnant liquid pool.[12] Unlike conventional mesh methods, these particle methods do not need to generate computational grids. The construction of interfaces between different phases is also unnecessary because each moving particle represents each phase with specific physical properties.

In this study, a computational framework is proposed to simulate the freezing and penetration behavior of solid-liquid mixture flows. The developed 3D computational code is based on FVP for fluid dynamics calculations coupled with distinct element method (DEM) for solid-phase interaction calculations. To validate the fundamental models employed in fluid dynamics, as well as heat and mass transfer calculations, a series of freezing experiments using pure molten metal (pure melt) was simulated using the developed 3D code. For solid-liquid mixture flows, the applicability of the present computational framework is thereby demonstrated by simulating the same for pure molten metal mixed with solid particles (mixed melt).

II. Physical Models and Numerical Methods

1. Governing Equations for Solid-Liquid Mixture Flows

The governing equations for the incompressible fluids are the Navier-Stokes equation and the continuity equation:

$$\frac{D\vec{u}_\mathrm{l}}{Dt} = \frac{1}{\rho_\mathrm{l}}\nabla P_\mathrm{l} + \frac{1}{\rho_\mathrm{l}}\nabla(\mu_\mathrm{l}\nabla\cdot\vec{u}_\mathrm{l}) + \frac{\vec{f}_\mathrm{sl}}{\rho_\mathrm{l}} + \frac{\vec{f}_\mathrm{others}}{\rho_\mathrm{l}}, \quad (1)$$

$$\nabla\cdot\vec{u}_\mathrm{l} = 0, \quad (2)$$

where $\vec{u}_\mathrm{l}$, P_l, ρ_l, and μ_l are the velocity, pressure, density, and dynamic viscosity of the liquid, respectively, $\vec{f}_\mathrm{sl}$ is the interaction force between liquid and solid phases per unit volume, and $\vec{f}_\mathrm{others}$ includes other volume forces per unit volume, such as gravity and surface tension force.

The movements of solid phase are obtained by solving the following governing equations:

$$m\frac{D\vec{u}_\mathrm{s}}{Dt} = \vec{F}_\mathrm{col} + \vec{f}_\mathrm{ls}V + \vec{F}_\mathrm{others}, \quad (3)$$

$$I\frac{D\vec{\omega}}{Dt} = \vec{\tau}_\mathrm{col} + \vec{\tau}_\mathrm{ls}, \quad (4)$$

where $\vec{u}_\mathrm{s}$, $\vec{\omega}$, m, V, and I are the translation velocity, rotation velocity, mass, volume, and inertia of a solid particle, and $\vec{F}$ and $\vec{\tau}$ are the force and torque, respectively. The subscripts "col" and "ls" stand for collisions between solid phases, and interactions between solid and liquid phases, respectively. It is noted that $\vec{f}_\mathrm{ls} = -\vec{f}_\mathrm{sl}$. The subscript "others" refers to other effects acting on the solid phase such as gravity.

The following energy equation that takes into account heat and mass transfer processes is solved mainly for the liquid and solid phases:

$$\rho\frac{DH}{Dt} = \nabla\cdot(k\nabla T) + Q, \quad (5)$$

where ρ is the density, H the specific internal energy, T the temperature, and Q the heat transfer rate per unit volume. The first term of the right-hand side of Eq. (5) represents the conductive heat transfer; the second term is the heat transfer at the interface between different phases.

In the present study, the surface tension force in Eq. (1) is formulated using a model based on the free surface energy.[13] The interactions between liquid and solid are evaluated by solving Eq. (1) even for the solid phase, which is represented by solid particles.[14] Equations (3) and (4) are solved using DEM. The phase-changing processes are assumed to be in nonequilibrium. In the following, we describe in detail the main physical models including FVP.

2. FVP Method

To discretize the governing equations for fluid, we choose FVP because it has been shown to be numerically stable, especially for free surface flow simulations.[15] FVP employs the same concept as conventional finite volume methods. It is assumed that each particle occupies a certain volume. The control volume of one moving particle is a sphere in 3D simulations:

$$S = 4\pi R^2,\ V = \frac{4}{3}\pi R^3 = (\Delta l)^3, \quad (6)$$

where S, V, R, and Δl are the particle surface area, particle control volume, radius of the particle control volume, and initial particle distance, respectively. According to Gauss's law, the gradient and Laplacian operators acting on an arbitrary scalar function ϕ are expressed as

$$\nabla\phi = \lim_{R\to 0}\frac{1}{V}\oint_V \nabla\phi dV = \lim_{R\to 0}\frac{1}{V}\oint_S \phi\vec{n}dS, \quad (7)$$

$$\nabla^2\phi = \lim_{R\to 0}\frac{1}{V}\oint_V \nabla^2\phi dV = \lim_{R\to 0}\frac{1}{V}\oint_S \nabla\phi\cdot\vec{n}dS, \quad (8)$$

where $\vec{n}$ is the unit vector. As a result, in FVP, the gradient and Laplacian terms can be approximated as

$$\langle\nabla\phi\rangle_i = \left\langle\frac{1}{V}\oint_S \phi\vec{n}dS\right\rangle_i = \frac{1}{V}\sum_{j\neq i}\phi_\mathrm{surf}\cdot\vec{n}_{ij}\cdot\Delta S_{ij}, \quad (9)$$

$$\langle\nabla^2\phi\rangle_i = \left\langle\frac{1}{V}\oint_S \nabla\phi\cdot\vec{n}dS\right\rangle_i = \frac{1}{V}\sum_{j\neq i}\left(\frac{\phi_j-\phi_i}{|\vec{r}_{ij}|}\right)\cdot\Delta S_{ij}, \quad (10)$$

where $\langle\phi\rangle_i$ is the approximation of ϕ with respect to particle i and $|\vec{r}_{ij}|$ is the distance between particles i and j. The function value ϕ_surf on the surface of particle i can be estimated using a linear function:

$$\phi_\mathrm{surf} = \phi_i + \frac{\phi_j-\phi_i}{|\vec{r}_{ij}|}R. \quad (11)$$

The unit vector of the distance between two particles, $\vec{n}_{ij}$, is defined as

$$\vec{n}_{ij} = \frac{\vec{r}_{ij}}{|\vec{r}_{ij}|}. \quad (12)$$

The interaction surface of particle i with particle j, ΔS_{ij}, can be calculated as

$$\Delta S_{ij} = \frac{\xi_{ij}}{n^0}S, \quad (13)$$

where the initial density, n^0, is defined as

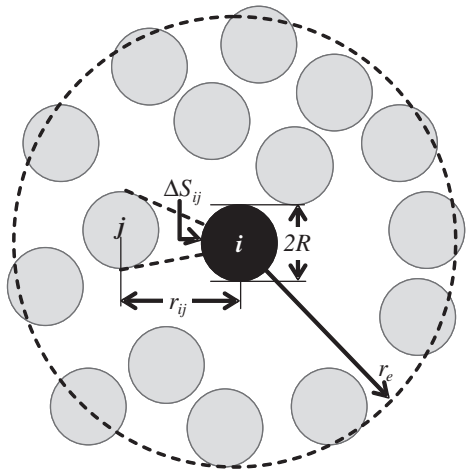

Fig. 1 Neighboring particles around particle i within the cut-off radius

$$n^0 = \sum_{j \neq i} \xi_{ij} \tag{14}$$

and the kernel function, ξ_{ij}, is defined as

$$\xi_{ij} = \sin^{-1}\left(\frac{R}{|\vec{r}_{ij}|}\right) - \sin^{-1}\left(\frac{R}{r_e}\right), \tag{15}$$

where r_e is the cut-off radius and is usually chosen as $2.1\Delta l$ for 3D systems. If the distance between two particles is larger than the cut-off radius, the kernel function is set to zero. A schematic diagram of neighboring particles around particle i within the cut-off radius is shown in **Fig. 1**.

Using Eqs. (11), (12), and (13), Eqs. (9) and (10) can be rearranged as

$$\langle \nabla \phi \rangle_i = \frac{S}{Vn^0} \sum_{j \neq i} \left(\phi_i + \frac{\phi_j - \phi_i}{|\vec{r}_{ij}|} R \right) \xi_{ij} \vec{n}_{ij}, \tag{16}$$

$$\langle \nabla^2 \phi \rangle_i = \frac{S}{Vn^0} \sum_{j \neq i} \frac{\phi_j - \phi_i}{|\vec{r}_{ij}|} \xi_{ij}. \tag{17}$$

Using the above gradient and Laplacian models, the governing equations for fluids can be easily discretized. These equations are then solved using the combined and unified procedure (CUP) algorithm;[16] a detailed explanation of this algorithm can be found in our previous study by Guo *et al.*[14]

3. Distinct Element Method

In the present study, DEM is utilized to calculate the collision force between solid particles and between solid particles and a solid wall. The solid particles and wall particles are represented by spherical particles of equal size. The translational and rotational motions of the solid particles are calculated using time-driven DEM.[17] Based on Eqs. (3) and (4), the motions of solid particle i are calculated using DEM as follows:

$$m_i \frac{d\vec{u}_i}{dt} = m_i \frac{d^2 \vec{x}_i}{dt^2} = \sum_{j \neq i} \vec{F}_{ij} + m_i \vec{g}, \tag{18}$$

$$I_i \frac{d\vec{\omega}_i}{dt} = I_i \frac{d^2 \vec{\theta}_i}{dt^2} = \sum_{j \neq i} \vec{d}_{cij} \times \vec{F}_{ij}, \tag{19}$$

where $\vec{x}_i$ and $\vec{\theta}_i$ are the respective vectors of position and orientation of the center of gravity of solid particle i, $\vec{F}_{ij}$ is the collision force between solid particle i and contacting solid and/or wall particle j, m_i and I_i the respective mass and inertia moment of solid particle i, $\vec{g}$ is the gravitational acceleration vector, and $\vec{d}_{cij} = -\vec{d}_{cji}$ are vectors specifying the position of the contact point with respect to the centers of the solid particles.

The evaluation of $\vec{F}_{ij}$ is presented by viscoelastic spherical particles, while the contact force between two particles i and j occurs due to elastic, viscous damping, and frictional effects. The particle interaction is modeled by a spring and dashpot in both the normal and tangential components $\vec{F}_{n,ij}$ and $\vec{F}_{t,ij}$:

$$\vec{F}_{ij} = \vec{F}_{n,ij} + \vec{F}_{t,ij}. \tag{20}$$

The normal component $\vec{F}_{n,ij}$ of the contact force depends on the contact geometry as well as on the physical properties of the particle's materials and is described by Hooke's law, taking into consideration the nonconservative viscous damping response during the collision

$$\vec{F}_{n,ij} = \frac{4}{3} \frac{E_i E_j}{E_i(1 - v_j^2) + E_j(1 - v_i^2)} R_{ij} h_{ij} \vec{n}_{ij} - \gamma_n m_{ij} \vec{v}_{n,ij}, \tag{21}$$

where $m_{ij} = \frac{m_i m_j}{m_i + m_j}$ and $R_{ij} = \frac{R_i R_j}{R_i + R_j}$ represent the reduced mass and reduced radius of particles i and j, respectively, E_i and E_j the elasticity moduli, and v_i and v_j the Poisson's ratios. In addition, $h_{ij} = R_i + R_j - |\vec{x}_{ij}|$ is the overlap between contacting particles i and j, where $\vec{x}_{ij}$ is the vector of a relative position of the two colliding particles, $\vec{n}_{ij}$ the unit vector normal to the contact surface and directed towards the particle i, $\vec{v}_{ij} = (\vec{v}_{ij} \cdot \vec{n}_{ij})\vec{n}_{ij}$ is the normal component of the contact relative velocity, and γ_n is the viscous damping coefficient in the normal direction.

The tangential force $\vec{F}_{t,ij}$ is specified by distinguishing between tangential forces produced by static or dynamic friction:

$$\vec{F}_{t,ij} = -\vec{t}_{ij} \min(|\vec{F}_{t,ij,\text{static}}|, |\vec{F}_{t,ij,\text{dynamic}}|), \tag{22}$$

where $\vec{t}_{ij}$ is the unit tangential vector.

The static friction force describes friction prior to gross sliding. The most general form is based on the assumption that static friction can be calculated as the sum of elastic and viscous damping components:

$$\vec{F}_{t,ij,\text{static}} = -\frac{16}{3} G_i G_j \sqrt{\frac{R_{ij} h_{ij}}{G_i(2 - v_j) + G_j(2 - v_i)}} \vec{\delta}_{ij} - \gamma_t m_{ij} \vec{v}_{t,ij}, \tag{23}$$

where $\vec{\delta}_{ij}$ is the integrated tangential displacement vector, G_i and G_j the respective shear moduli, $\vec{v}_{t,ij} = \vec{v}_{ij} - \vec{v}_{n,ij}$ the tangential relative velocity of the colliding particles i and j, and γ_t the viscous damping coefficient in the tangential direction.

The dynamic friction force describes friction after gross sliding and is expressed by the Coulomb law as follows:

$$\vec{F}_{t,ij,\text{dynamic}} = -\eta |\vec{F}_{n,ij}| \vec{t}_{ij}, \tag{24}$$

where η is the friction coefficient.

In calculating the collision force using DEM, it is generally accepted that the DEM time step size should be less than a certain critical value. The common relational form for time step size is that defined using the particle mass and stiffness:[18)]

$$\Delta t_c \leq C\sqrt{m/k}, \tag{25}$$

where C is a constant. In general, the time step size for DEM calculations could be much smaller than that for the fluid dynamic calculations based on the semi-implicit solution algorithm. In this study, to couple DEM with the fluid dynamic calculation, a multiple time-step scheme is applied.[11)]

4. Heat and Mass Transfer Model

Phase changing processes are based on a nonequilibrium model[19)] that calculates the mass transfer occurring at the interface between solid and liquid phases. For interfaces where no phase change is predicted, only the first term on the right-hand side of Eq. (5) is included. By the Lagrangian discretization modeled using Eq. (10), it is approximated as

$$\langle \nabla \cdot (k \nabla T) \rangle_i \simeq \frac{1}{V} \sum k_{ij} \frac{T_j - T_i}{|\vec{r}_{ij}|} \Delta S_{ij}, \tag{26}$$

where the thermal conductivity k_{ij} between particles i and j is defined as

$$k_{ij} = \frac{2k_i k_j}{k_i + k_j}. \tag{27}$$

The thermal conductivity k_i of particle i is simply approximated as

$$k_i = (1 - \alpha_{l,i}) k_{s,i} + \alpha_{l,i} k_{l,i}, \tag{28}$$

where $k_{s,i}$ and $k_{l,i}$ are the solid and liquid thermal conductivities of particle i, respectively, and $\alpha_{l,i}$ is the volume fraction of the liquid phase in particle i.

For the interface of particle i where a phase change is predicted, the second term on the right-hand side of Eq. (5) is calculated as

$$Q_{i,j} = a_{ij} h_i (T_{ij}^{I} - T_i), \tag{29}$$

where the heat transfer coefficient depends on the thermal conductivity of particle i:

$$h_i = 2 \frac{k_i}{|\vec{r}_{ij}|} \tag{30}$$

and T_{ij}^{I} is defined as either $T_{ij}^{I} = \min[T_{liq}, \max(T_{ij}^{N}, T_{sol})]$ for solid-liquid interface, or $T_{ij}^{I} = \max(T_{ij}^{N}, T_{sol})$ for solid-wall interface, where no phase change is assumed. T_{liq} and T_{sol} are the liquidus and solidus temperatures, respectively; T_{ij}^{N} is defined as the temperature for sensible heat transfer:

$$T_{ij}^{N} = \frac{h_i T_i + h_j T_j}{h_i + h_j}. \tag{31}$$

The net heat flow rate at the interface is given by

$$Q_{i,j}^{I} = Q_{i,j} + Q_{j,i}. \tag{32}$$

Once the net heat flow rate Q_{ij}^{I} is determined, the melting/freezing rate can be calculated. If $Q_{ij}^{I} > 0$ and the particle i contains a liquid phase, it will freeze partly into a solid phase; its freezing rate is calculated as

$$\Gamma_{i,\text{freezing}} = \sum_{j \neq i} \frac{Q_{ij}^{I}}{H_f}, \tag{33}$$

where H_f is the latent heat of fusion. If $Q_{ij}^{I} < 0$ and particle i contains a solid phase, it will partially melt into a liquid phase; its melting rate is calculated as

$$\Gamma_{i,\text{melting}} = -\sum_{j \neq i} \frac{Q_{ij}^{I}}{H_f}. \tag{34}$$

Otherwise, only sensible heat will be exchanged between particles i and j by applying T_{ij}^{N} to the interface. Using Eqs. (33) and (34), the liquid and solid masses of particle i can be updated as

$$\begin{aligned} m_{l,i}^{n+1} &= m_{l,i}^{n} + \Delta t(\Gamma_{i,\text{melting}} - \Gamma_{i,\text{freezing}}), \\ m_{s,i}^{n+1} &= m_{s,i}^{n} + \Delta t(\Gamma_{i,\text{freezing}} - \Gamma_{i,\text{melting}}), \end{aligned} \tag{35}$$

where $m_{l,i}$ and $m_{s,i}$ are the liquid and solid masses of particle i, respectively, Δt is the time step size of the fluid dynamics calculation, and the superscript n is an iterative index for the n-th time step of the calculation. Equation (35) can be used to determine the volume fraction of the liquid phase in particle i, which is necessary in evaluating its mixture thermal conductivity from Eq. (28).

5. Viscosity Model

In simulations of solid-liquid mixture flows, the rheological behavior has a significant influence on not only heat and mass transfer but also the dynamics of the solid and liquid during melting and freezing. In the present study, it is considered by estimating the viscosity of the liquid phase with its compositional development. Based on our previous study,[20)] the viscosity model that takes into account viscosity changes due to phase changes is expressed using the following empirical approximation:

$$\mu_{\text{app},i} = \min\left(\mu_{\max}, \mu_l \exp\left[-\frac{A(H_i - H_{liq})}{C_p}\right]\right), \tag{36}$$

where $\mu_{\text{app},i}$ is the dynamic viscosity of particle i during melting and freezing, which is in Eq. (1) instead of μ_l, H_{liq} is the specific enthalpy at the liquidus point, and A is the rheology parameter with unit of K^{-1}, the value of which will be determined by comparing the simulation results with those of pure-melt freezing experiments. The upper limit value, $\mu_{\max}$, is introduced to maintain numerical stability:

$$\mu_{\max} = \mu_l \exp\left[-\frac{A(H_{\alpha=0.375} - H_{liq})}{C_p}\right], \tag{37}$$

where $H_{\alpha=0.375}$ is the enthalpy at a liquid volume fraction $\alpha = 0.375$.[21)]

III. Experimental Setup

Figure 2 shows a schematic diagram of the experimental apparatus that was used in both pure- and mixed-melt freezing experiments. The apparatus consists of a melt tank and a flow channel. In the pure melt freezing experiments, we used the low-melting-point Wood's metal as the molten metal

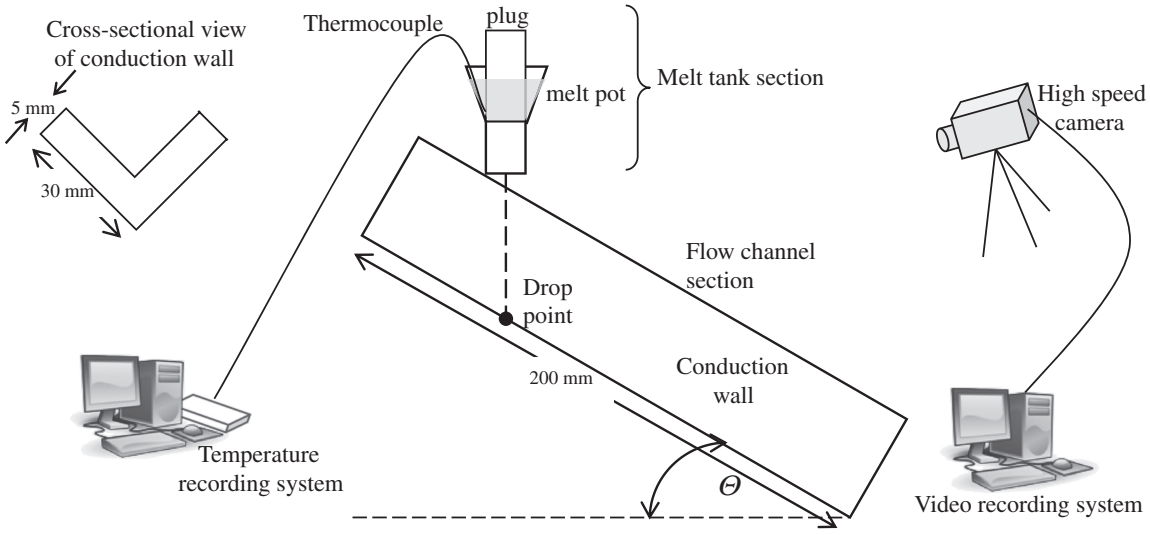

Fig. 2 Experimental apparatus

Table 1 Material properties of Wood's metal and solid particles

Properties	Wood's metal		Brass	Copper
	Solid	Liquid	(Solid)	(Solid)
Melting point [°C]	78.8		875	1,082
Latent heat of fusion [kJ/kg]	47.3		168	205
Density [kg/m^3]	8,528	8,528	8,470	8,940
Specific heat [J/(kg·K)]	168.5	190	377	385
Viscosity [Pa·s]	—	2.4×10^3	—	—
Conductivity [W/(m·K)]	9.8	12.8	117	403

Table 2 Conditions of pure-melt freezing experiments

Case	P-1	P-2	P-3	P-4
Wall material	Brass	Copper	Copper	Copper
Inclination angle, Θ	30°	30°	30°	15°
Initial melt temperature	82.1°C	81.6°C	82.4°C	82.6°C
Melt volume, V_m	2 cm^3	1.5 cm^3	2 cm^3	2 cm^3

material. In the mixed melt experiment, a mixture of molten Wood's metal and solid copper particles of 1 mm diameter was used to observe the effects of solid particles on melt penetration and freezing behavior. The choice of this particle material is attributed to the wettability between copper and the molten Wood's metal.

The melt tank consists of a pot and a plug, both made of Teflon. The pot's neck has a 4 cm length and its upper and lower inner diameters are 0.88 and 0.6 cm, respectively. The cylindrical plug is 20 cm long with a 1.4 cm outer diameter, except at the edge of the plug that contacts the upper part of the pot's neck, where it has the same diameter as the upper neck to prevent leakage of the melt into the tank. The flow of the melt onto the flow channel is enabled by raising the plug. The pouring rate was not measured in the experiments, and hence, the pouring is assumed to occur under the free fall condition. The flow channel section is an L-shaped conduction wall made of brass or copper inclined at a certain angle to enable flow along the channel. As shown in Fig. 2, the dimension of the L-shaped wall was $20.0 \times 3.0 \times 0.5$ cm in length, width, and thickness, respectively. The inclination angle of the conduction wall is set to 15 and 30° to the horizontal. Relevant material properties of Wood's metal, brass, and copper are listed in **Table 1**.

In preparing the experiment, the melt is heated above the desired temperature in the range of 80–88°C for melt release, and then transferred to the pot. When the temperature of the melt in the pot has reached the desired temperature, the plug is extracted and the melt is allowed to discharge from the pot onto the conduction wall.

During the experiments, temperatures in the pot and at the drop point onto the conduction wall (see Fig. 2) are measured using thermocouples. A high-speed camera is used to record the transient behavior of the melt and to measure its penetration length along the conduction wall until the melt has completely frozen. Freezing takes about 0.2–0.8 s. A series of experiments was conducted with various parameters, *i.e.*, wall material, inclination angle, melt volume, and solid particle volume fraction. Conditions for the pure- and mixed-melt freezing experiments are summarized in **Tables 2** and **3**, respectively.

IV. Simulation Result and Discussion

1. Simulation Setup and Boundary Conditions

In the present 3D simulations of both pure- and mixed-melt freezing experiments, the initial particle distance Δl was set to 1 mm, and the time step size was 0.1 ms. **Figure 3** shows the channel geometry for the present simulations. With the initial particle distance of 1 mm, one moving particle has a volume of 10^{-3} cm^3, and hence, the pure and mixed melts are represented by 1,500–2,000 moving particles, depending on the melt volume. The conduction wall is represented by an array of $200 \times 30 \times 5$ moving particles corresponding to the length, width and thickness, respective-

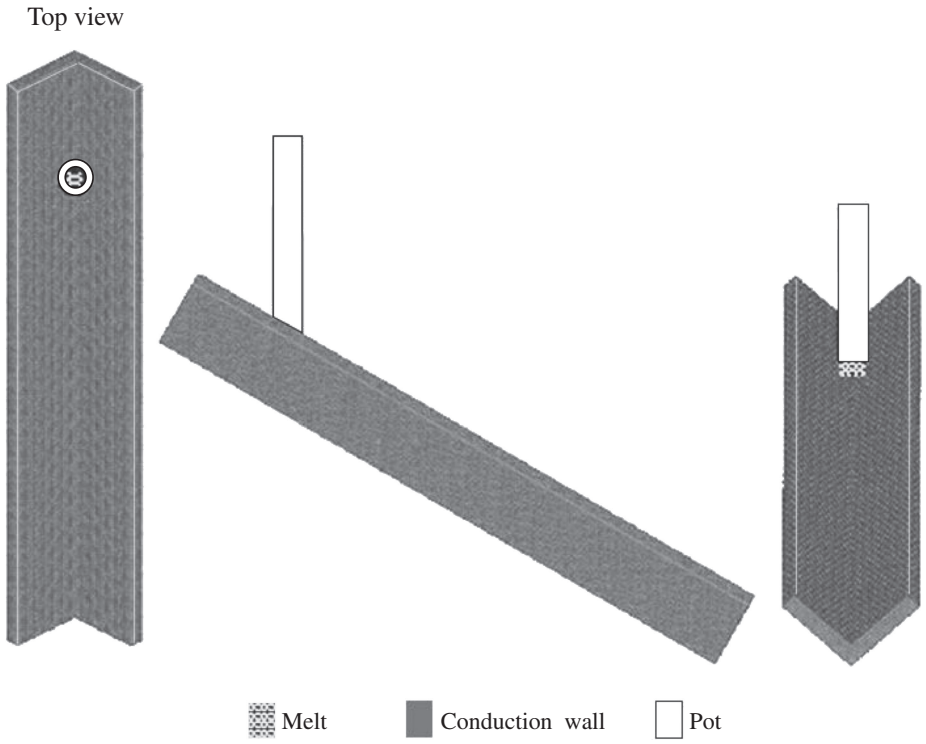

Fig. 3 Geometrical setup of simulation

Table 3 Conditions of mixed-melt freezing experiments

Case	M-1	M-2	M-3
Wall material	Brass	Copper	Brass
Solid volume fraction, α_p	17.5%	20%	20%
Inclination angle, Θ	30°	30°	15°
Initial melt temperature	87.3°C	86.4°C	85.1°C
Mixed-melt volume, V_m	1.5 cm^3	2 cm^3	2 cm^3

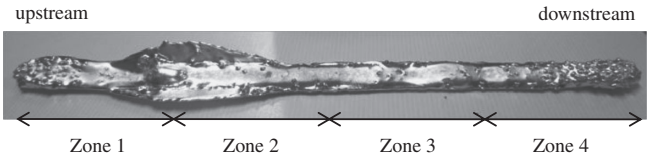

Fig. 4 An example of frozen melt and zone definition

ly. Only the first two layers of the wall particles are used as boundary particles for the fluid dynamic calculation because $2.1\Delta l$ is chosen for the cut-off radius r_e. In the heat conduction calculation, all the wall particles are involved in simulating the heat transfer from the melt to the wall. The present simulations did not model the heat transfer from the melt and the wall to the surrounding air because its effect on melt penetration and freezing behavior should be negligibly small over the short time period that the present experiments take.

The boundary treatment in the fluid dynamics and DEM calculations are as follows:

(1) In FVP, we have taken the zero Dirichlet condition for pressure and homogeneous Neumann condition for velocity divergences in determining the pressure for particles on the free surface.[20)]
(2) For the DEM simulation, a stationary plane wall describing the geometrical configuration of the conduction wall is applied.

To validate the fluid dynamic models for freezing behavior of melt flows on a cold structure wall, the measured transient penetration length and mass distribution of frozen molten metal are compared with simulation results. Here, the penetration length is defined as the length of the melt on the conduction wall as measured from the drop point. The mass distribution in the direction of the longitudinal length of the wall was measured for the four equal-length zones of the frozen melt. In the mixed-melt experiments, we also measured the mass of solid particles in each zone. An example of the frozen melt and zone definition is presented in **Fig. 4**.

To validate the applicability of the fluid dynamics and the heat and mass transfer models in simulating melt flows undergoing solidification, the simulation of pure-melt freezing experiments was performed first. The validated models coupled with DEM were then applied to mixed-melt freezing experiments, which were performed to measure the mixture penetration and freezing behavior under the influence of the solid particles.

2. Pure Melt Freezing Simulation

To simulate the freezing behavior of the melt on the cold structure, it is necessary to determine the rheology parameter A appearing in Eq. (36). Its optimization was performed by carrying out certain parametric calculations of the pure-melt freezing experiment, labeled as Case P-1. **Figure 5** shows

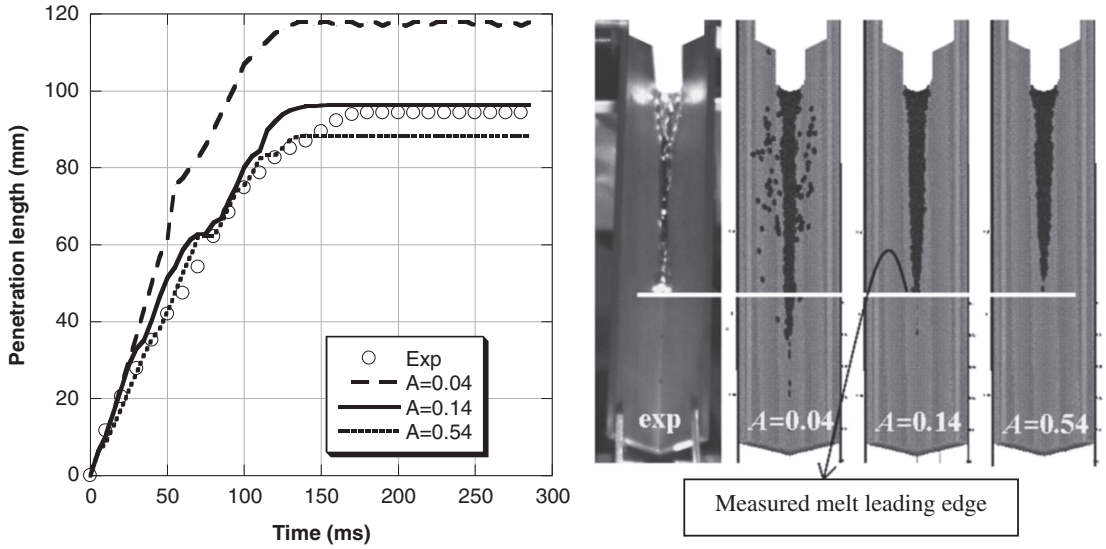

(a) transient penetration length (b) frozen melt on the wall

Fig. 5 Comparison of pure-melt penetration between simulations using a different rheology parameter A and experiment (Case P-1: brass wall; $\Theta = 30^\circ$; $V_m = 1.5\,cm^3$)

the simulation results of transient penetration length and frozen-melt shape with different rheology parameters in the range of 0.04–0.54. In the simulation results, which are indicated by the right three images, the gray and black colors indicate the conduction wall and the Wood's metal, respectively. The white-colored parts, which represent the melt pot, are intentionally added to make visual comparisons easier. As can be seen in Fig. 5(b), unlike the experiment, the simulation result with $A = 0.04$ shows an apparently dispersive distribution of the melt on the wall. By comparing the shape of the frozen melt and the transient penetration length between the experiment and simulation, we found $A = 0.14$ as a reasonable value for the rheology parameter.

To validate the applicability of the rheology model with this optimized parameter, further pure melt freezing experiments were simulated with a copper conduction wall, labeled as Cases P-2, P-3, and P-4. **Figure 6** shows the penetration length in these three cases. The simulation results for penetration behavior show fairly good agreement with the experiments. In the initial stages, the transient penetration length increases rapidly and then after a certain time the increase in penetration gradually reduces until the melt completely freezes (no change in the penetration length). The rapid increase in penetration length in the initial stage is due to melt impacting with the conduction wall. The initial velocity of the melt in the pot is set to zero and is allowed to fall gravitationally. Given this impact velocity, melt penetration develops rapidly in the initial stages. However, on reaching the wall, heat transfer from the hot melt to the cold conduction wall occurs. Due to the rheological effect of the melt, the resulting temperature decrease leads to an increase in the viscosity force, which suppresses the melt velocity. The slower melt movement will lead to a smaller change in penetration length. When melt temperatures reach the freezing point, the melt viscosity becomes very large and the melt will completely stop penetrating along the wall. For this reason, the heat and mass transfer model as well as the viscosity model play important roles in representing the transient behavior of melt penetration, which is reasonably reproduced by the present simulations. In addition, the simulated freezing time, *i.e.*, the time taken for the melt to stop flowing on the wall, agrees well with the measurements.

The results of frozen-melt mass distribution in Cases P-1, P-2, P-3, and P-4 are shown in **Fig. 7**. As can be seen in Fig. 7, the comparison between experiments and simulations shows good agreement. All the cases indicate the same tendency for the mass distribution. Much more of the melt freezes in Zones 1 and 2, while Zone 4 yields the smallest amount of frozen mass. Approximately 70–75 vol% of the melt freeze in Zones 1 and 2 is due to the rapid heat transfer just after the melt impact on the wall and the resultant viscosity change. The remaining melt will flow along the wall with a slower velocity due to the viscosity increase.

The present simulation results for pure-melt freezing experiments demonstrate that the fluid dynamic models employed in the developed 3D code, in particular, the heat and mass transfer models and the viscosity model, can reproduce the fundamental freezing behaviors that are observed from the melt penetration length and the frozen mass distribution under the various experimental conditions imposed.

3. Mixed-Melt Freezing Simulation

(1) DEM Effects

To validate the effectiveness of DEM in solid-liquid mixture freezing simulations, the simulation results of the mixed-melt freezing experiment, Case M-1, were compared with calculations using DEM and without DEM. It is noted that the calculation without DEM includes only the interactions between liquid and solid as the effects of solid particles. Therefore, this comparison enables us to understand the effects of interactions between solid phases on melt penetration and freezing behavior. The properties of solid copper

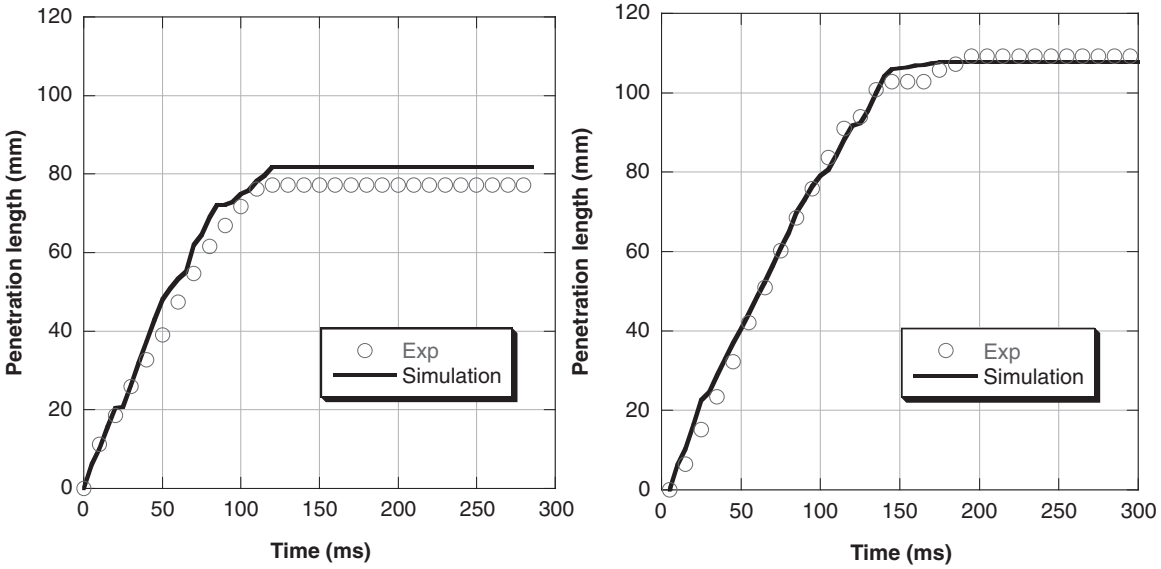

(a) Case P-2 ($\Theta = 30°$; $V_m = 1.5$ cm^3)

(b) Case P-3 ($\Theta = 30°$; $V_m = 2$ cm^3)

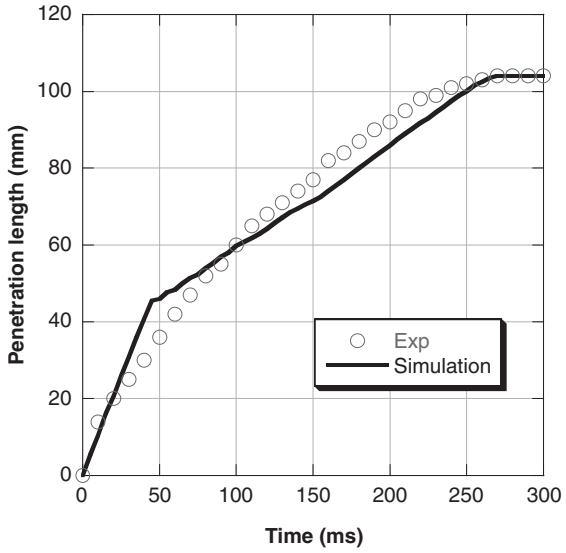

(c) Case P-4 ($\Theta = 15°$; $V_m = 2$ cm^3)

Fig. 6 Comparison of transient penetration length between simulation and experiment in the cases of pure melt (Cases P-2, P-3, and P-4: copper wall)

Table 4 Properties of solid copper particles

Properties	
Density [kg/m^3]	8,940
Poisson's ratio	0.34
Elasticity modulus [Pa]	117×10^9
Shear modulus [Pa]	48×10^9

particles used in the calculations are listed in **Table 4**. In the present calculations, DEM parameters, *viz.* friction coefficient, and normal and tangential damping coefficients, were optimized by experimental analysis and were set to 0.2, 60, and 10 s^{-1}, respectively.

The transient penetration length and mass distribution of solid particles in the frozen melt from both experiments and simulations are compared in **Fig. 8**, with and without DEM. The simulation result with DEM shows fairly better agreement than those without DEM. Without DEM, the simulation shows a longer penetration length than actual measurements. This is because, just after the mixed-melt begins to flow along the conduction wall, separation starts to occur for some solid particles from the bulk mixed melt. The solid particles then separately move faster than the bulk melt because they are not affected by the viscosity changes due to heat transfer. Thus, the mass of solid particles involved in the mixed melt becomes smaller than the initial solid one.

In contrast, in the simulation with DEM, the collision forces acting between solid particles and between solid particles and the wall will reduce the whole momentum of solid particles, and hence, their movement would be slower than that in the simulation without DEM. As a result, the solid

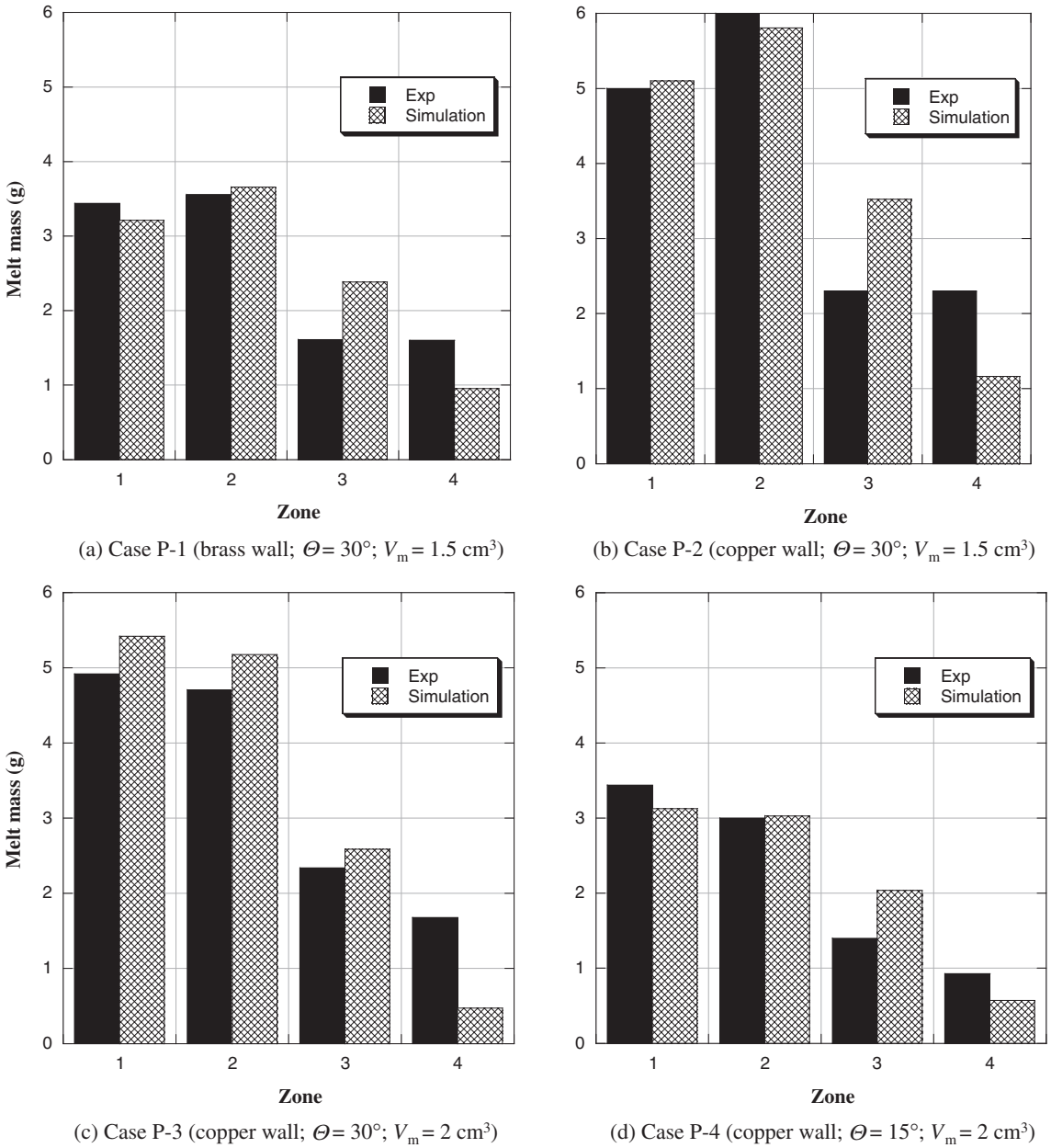

(a) Case P-1 (brass wall; $\Theta = 30°$; $V_m = 1.5$ cm^3)

(b) Case P-2 (copper wall; $\Theta = 30°$; $V_m = 1.5$ cm^3)

(c) Case P-3 (copper wall; $\Theta = 30°$; $V_m = 2$ cm^3)

(d) Case P-4 (copper wall; $\Theta = 15°$; $V_m = 2$ cm^3)

Fig. 7 Comparison of frozen-melt mass distribution in the cases of pure melt (Case P-1, P-2, P-3, and P-4)

particles tend to move together with the bulk melt and their separation is difficult to occur. The conclusion is that the penetration length of the mixed melt can be reasonably reproduced in simulations with DEM.

The effectiveness of DEM can also be seen from the distribution of solid particles. The solid particle distribution in the experiments and the simulation results with DEM have a similar tendency. **Figure 9** shows a visual comparison of the frozen melt on the structure surface between simulation results with and without DEM. In this figure, the black and white colors indicate Wood's metal and the solid copper particles, respectively. The solid particles mainly gathered in Zone 4 in the simulation with DEM as well as the experiment, while the simulation without DEM shows the opposite result. This is caused by the separation of solid particles from the bulk of the mixed melt because, as described before, most of the solid particles flow out of the channel without freezing with the melt.

From the above comparison of the penetration length and the mass distribution of solid particles between the simulation results with and without DEM, we can conclude that DEM is reasonably useful in representing the effects of solid particles mixed with molten metal on mixture freezing behavior. Hereafter, the mixed-melt freezing flow simulations will be performed using the developed 3D code with DEM.

(2) Simulation Results

The conditions in the various mixed-melt freezing simulations performed in the present study are summarized in Table 3. **Figure 10** shows visual comparisons of the freezing process between the experiment and simulation results for Case M-1. As can be seen in this figure, where the simulation results are indicated on the left side for each

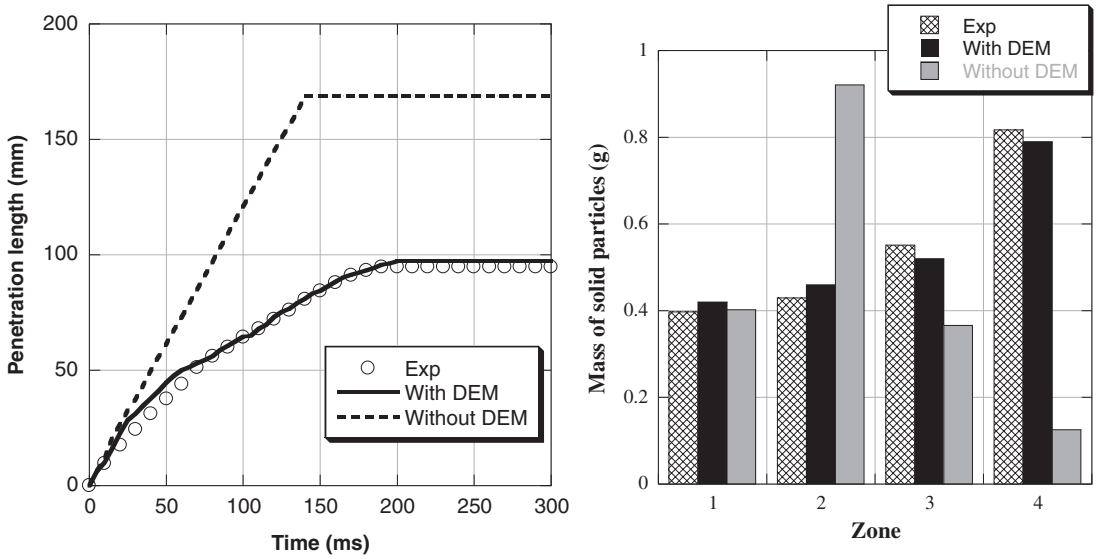

(a) Transient penetration length (b) Mass distribution of solid particles

Fig. 8 Comparison of mixed-melt freezing behavior between simulations with and without DEM (Case M-1: brass wall; $\Theta = 30^\circ$; $\alpha_p = 17.5\%$, $V_m = 1.5\,cm^3$)

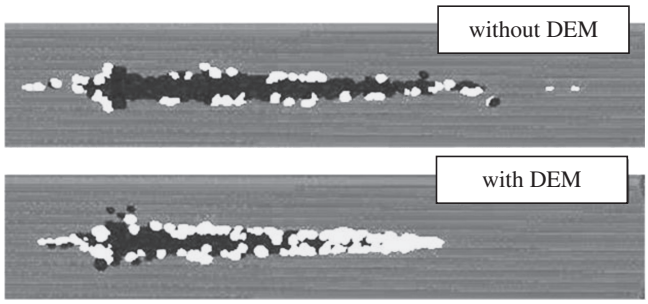

gray : wall; black : melt; white : solid copper particles

Fig. 9 Comparison of visualization results for frozen mixed melt between simulations with and without DEM (Case M-1)

instant of time, the simulation and experimental results indicate reasonable agreement in the shape of the mixtures during freezing onto the wall. The penetration lengths of the mixture measured in the experiment are also reasonably reproduced by the present simulation, although it is hard to compare the solid particle distribution in the mixture in every instant of time qualitatively due to the limitation of photographic results in the experiment.

In the experiments, the freezing process of the mixture has a similar tendency in all the cases. When the mixed melt reaches and starts flowing on the wall, the melt will eventually freeze and penetrate along the wall, while the solid copper particles will continue to flow until the surrounding melt freezes. Thus, Fig. 10 shows that the solid copper particles have a tendency to gather at the leading edge (Zone 4) of the frozen mixture. This is because the solid copper particles will continue to flow with the melt until it completely freezes. This behavior can be explained quantitatively from the mass distribution of the melt and solid copper particles, as discussed below.

The comparisons of the mass distribution of the frozen melt between experiments and simulations are shown for Cases M-2 and M-3 in **Fig. 11**. As can be seen in this figure, the mass distribution of the melt in each zone shows good agreement between the experiment and simulation. The distribution of the melt, as has been discussed in those cases of just pure-melt freezing, concentrates mainly in Zones 1 and 2. With the copper wall (Case M-2), Zones 1 and 2 have a larger mass than the other zones, while with the brass wall (Case M-3), the mass in Zone 2 turns out to be the largest. This difference can be explained by the different heat transfer rate to the wall (copper has about 3.5 times larger thermal conductivity than brass). Regardless of the inclination of the conduction wall, the mixed melt will move not only downward but also upward just after it impacts the wall. Due to the high thermal conductivity of copper, the melt that moves in the upwards direction freezes instantly in Zone 1; in comparison with the brass wall, melt freezing develops more slowly. Thus, the melt that once moves in an upward direction will begin to flow downstream due to gravity without freezing and will eventually freeze in Zone 2.

The mass distribution of solid copper particles in the frozen melt is compared between the experiment and simulation results for Cases M-2 and M-3 in **Fig. 12**. As discussed above in Case M-1, the solid copper particles in both these cases are always found to concentrate in Zone 4, basically because these will continue to flow until the surrounding melt freezes. With the copper wall (Case M-2), the zone that has the second largest particle mass is Zone 1, while with the brass wall (Case M-3), this is Zone 3. This tendency can also be explained by the different heat transfer rates to the wall as discussed above. Due to the higher density of the solid copper particles than that of Wood's metal, the solid copper particles accumulate in the lower part

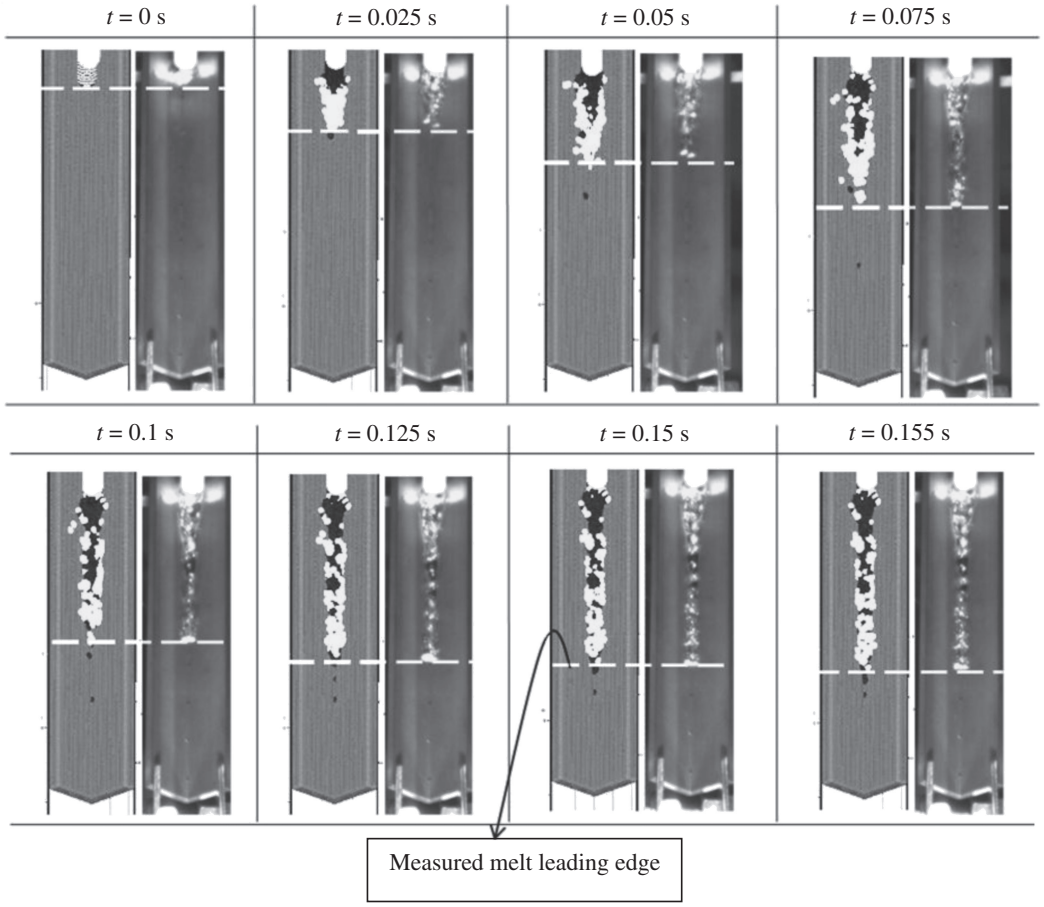

Fig. 10 Comparison of visualization results for transient freezing behavior of mixed melt between simulation and experiment (Case M-1)

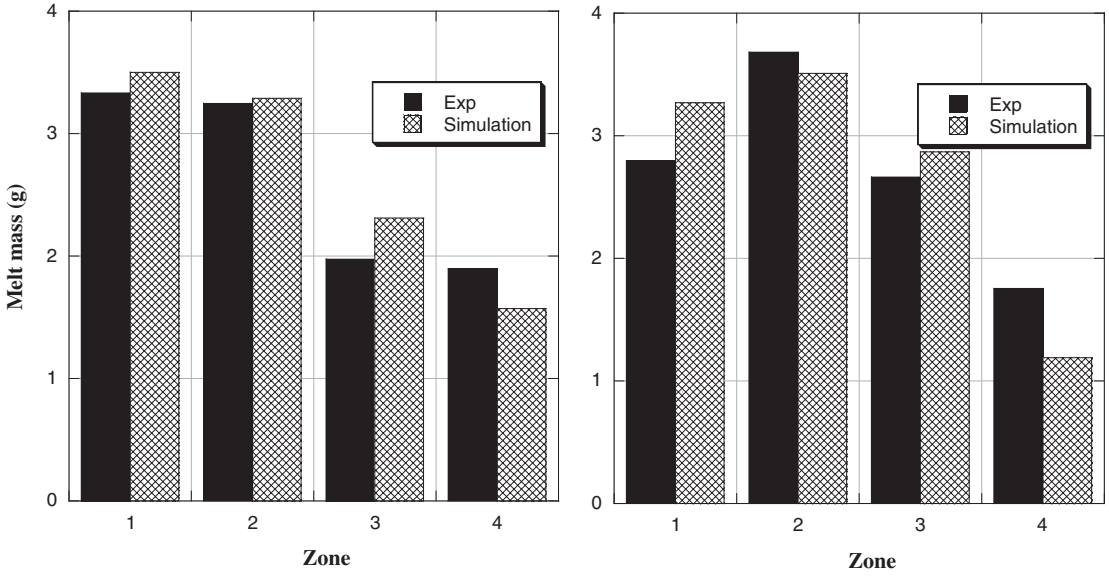

(a) Case M-2 (copper wall; $V_m = 2$ cm^3) (b) Case M-3 (brass wall; $V_m = 2$ cm^3)

Fig. 11 Comparison of frozen-melt mass distribution in the cases of mixed melt (Cases M-2 and M-3; $\alpha_p = 20.0\%$)

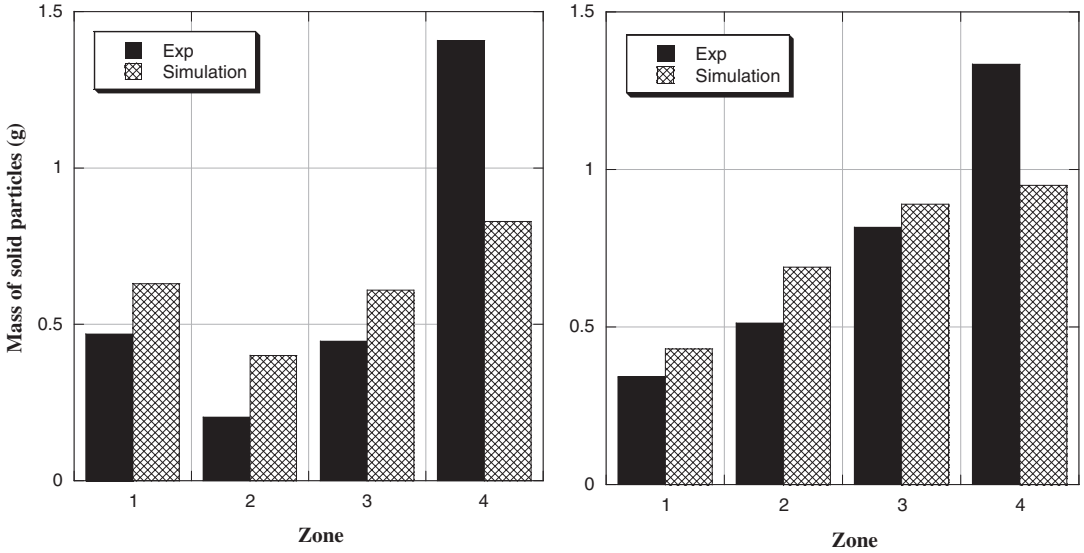

(a) Case M-2 (copper wall; $V_m = 2$ cm^3) (b) Case M-3 (brass wall; $V_m = 2$ cm^3)

Fig. 12 Comparison of solid particle mass distribution in the cases of mixed melt

of the mixture before melt release, and as a consequence, a particle-rich mixture will impact the wall first. With the copper wall, instant freezing makes the solid particles dense in Zone 1; in contrast, with the brass wall, the particle-rich mixture freezes as it reaches Zone 3, due to the relatively slower heat transfer. As a result, the frozen mixed melt contains much solid particles toward its leading edge in the downward direction.

The above three simulation results for mixed-melt freezing reproduce the typical characteristics of some observed mixed-melt freezing behaviors depending on the experimental conditions. This demonstrates the applicability of the present fluid dynamics models coupled with DEM to the simulation of solid-liquid mixture freezing behavior under the influences of solid particles in the mixture.

V. Conclusion

In this study, to simulate the freezing behavior of solid-liquid mixture flows on a structure, a computational framework was proposed using the finite volume particle (FVP) method coupled with the distinct element method (DEM), which was employed to model interaction forces between solid phases. The fundamental models for the fluid-dynamics behaviors including melt rheology and heat and mass transfers were validated using a series of pure-melt freezing experiments. For the freezing behavior of solid-liquid mixture flows, the developed 3D fluid dynamics code indicates that DEM can significantly improve the simulation results. By simulating the mixed-melt freezing experiments, the validity of the developed code was demonstrated for various thermal and hydraulic conditions under solid particle influences. It can be concluded that the developed computational framework based on the FVP method coupled with DEM can reasonably represent the freezing process of solid-liquid mixture flows on a structure.

Acknowledgements

The corresponding author, Rida SN Mahmudah, gratefully acknowledges the support from the Ministry of Education, Culture, Sports, Science and Technology of Japan under the Monkagakusho scholarship. The computation was mainly performed using the computer facilities at the Research Institute for Information Technology, Kyushu University. Finally, the authors would like to thank Mr. W. Torii, Mr. I. Miya and Mr. T. Takeda for their kind help in conducting the experiments.

Nomenclature

A: rheology parameter [K^{-1}]
a_{ij}: contact area of particle i and j interface per unit volume [m^{-1}]
$\underrightarrow{C}_p$: specific heat capacity [J/(kg·K)]
$\vec{d}$: vector position of contact point
E: elasticity modulus [Pa]
G: shear modulus [Pa]
$\vec{F}$: force [N]
$\vec{f}$: force per unit volume [N/m^3]
$\vec{g}$: gravity [m/s^2]
H: specific enthalpy [J/kg]
H_f: latent heat of fusion [J/kg]
H_{liq}: specific enthalpy at liquidus point [J/kg]
h: heat transfer coefficient [W/(m^2·K)]
I: inertia of particle [kg·m/s]
k: thermal conductivity [W/(m·K)]
Δl: initial particle distance [m]
m: mass [kg]
n^0: initial number density of the particles
$\vec{n}$: unit vector
P: pressure [Pa]
Q: heat transfer rate per unit volume [W/m^3]
Q^I_{ij}: heat transfer rate at interface of particle i and j per unit volume [W/m^3]

R: radius of control volume [m]
r_e: cut-off radius [m]
r: liquid particle's position [m]
S: surface of control volume [m^2]
ΔS: interaction surface [m^2]
T: temperature [K]
T_{liq}: liquidus temperature [K]
T_{sol}: solidus temperature [K]
t: time [s]
$\vec{t}$: unit tangential vector
Δt: time step size [s]
T_{ij}^{I}: interface temperature of particle i and j [K]
u: particle's velocity [m/s]
V: volume [m^3]
$\vec{v}$: contact relative velocity [m/s]
$\vec{x}$: solid particle's position [m]

Greek Letters

α: liquid volume fraction
ρ: density [kg/m^3]
μ: dynamic viscosity coefficient [Pa·s]
μ_{app}: dynamic viscosity coefficient during phase change [Pa·s]
Γ: mass transfer rate per unit volume [$kg/(m^3 \cdot s)$]
η: friction coefficient
$\vec{\theta}$: angular position of solid particle [rad]
$\vec{\delta}$: integrated tangential displacement vector
ϕ: arbitrary scalar function
ξ: kernel function
$\vec{\omega}$: particle's angular velocity [rad/s]
γ: viscous damping coefficient [1/s]
υ: Poisson's ratio
$\vec{\tau}$: torque [N·m]

Subscripts

i: particle i
j: particle j
ij: between two contacting particles i and j
l: liquid
s: solid
surf: surface
ls: liquid-solid
sl: solid-liquid
n: normal direction
t: tangential direction
col: collision
static: static component of friction force
dynamic: dynamic component of friction force

References

1) Sa. Kondo, K. Konishi, M. Isozaki *et al.*, "Experimental study on simulated molten jet-coolant interaction," *Nucl. Eng. Des.*, **204**, 377–389 (1995).
2) W. Peppler, A. Kaiser, H. Will, "Freezing of a thermite melt injected into an annular channel experiments and recalculations," *Exp. Therm. Fluid Sci.*, **1**[4], 335–346 (1988).
3) M. M. Rahman, Y. Ege, K. Morita *et al.*, "Simulation of molten metal freezing behavior on to a structure," *Nucl. Eng. Des.*, **238**, 2706–2717 (2008).
4) M. K. Hossain, Y. Himuro, K. Morita *et al.*, "Simulation of molten metal penetration and freezing behavior in a seven-pin bundle experiment," *Nucl. Sci. Technol.*, **46**[8], 799–808 (2009).
5) Sa. Kondo, Y. Tobita, K. Morita *et al.*, "SIMMER-III: An advanced computer program for LMFBR severe accident analysis," *Proc. Int. Conf. on Design and Safety of Advanced Nuclear Power Plant* (ANP '92), Tokyo, Japan, Oct. 25–29, 1992, IV, 40.5-1 (1992).
6) Y. Tobita, Sa. Kondo, H. Yamano *et al.*, "Current status and application of SIMMER-III, an advanced computer program for LMFR safety analysis," *Proc. Second Japan-Korea Symp. on Nuclear Thermal Hydraulics and Safety (NTHAS2)*, Fukuoka, Japan, Oct. 15–18, 2000, 65 (2000).
7) J. Monaghan, "Smoothed particle hydrodynamics," *Rep. Prog. Phys.*, **68**, 1703–1759 (2005).
8) S. Koshizuka, Y. Oka, "Moving-particle semi-implicit method for fragmentation of incompressible fluid," *J. Nucl. Sci. Eng.*, **123**, 421 (1996).
9) K. Yabushita *et al.*, "A finite volume particle method for an incompressible fluid flow," *Proc. Comp. Eng. Conf.*, **10**, 419–421 (2005), [in Japanese].
10) S. Koshizuka, H. Ikeda, Y. Oka, "Numerical analysis of fragmentation mechanisms in vapor explosions," *J. Nucl. Eng. Des.*, **189**, 423–433 (1998).
11) S. Zhang, S. Kuwabara, T. Suzuki *et al.*, "Simulation of solid-fluid mixture using moving particle methods," *J. Comp. Phys.*, **228**, 2552–2565 (2009).
12) S. Zhang, L. Guo, K. Morita *et al.*, "Simulation of single bubble rising up in stagnant liquid pool with finite volume particle method," *Proc. Sixth Japan-Korea Symp. on Nuclear Thermal Hydraulics and Safety (NTHAS6)*, Okinawa, Japan, Nov. 24–27, 2008, N6P1022 (2008).
13) M. Kondo, K. Suzuki, S. Yoshizuka *et al.*, "Surface tension model using inter-particle force in particle method," *FEDSM 2007 I Symposia (Part A)*, San Diego, USA, Jul. 30–Aug. 2, 2007, 93–98 (2007).
14) L. Guo, S. Zhang, K. Morita *et al.*, "Fundamental validation of the finite volume particle method for 3D sloshing dynamics," to be published in *Int. J. Numer. Methods Fluids*.
15) S. Zhang, K. Morita, K. Fukuda *et al.*, "A new algorithm for surface tension model in moving particle methods," *Int. J. Numer. Methods Fluids*, **55**, 225–240 (2007).
16) F. Xiao, T. Yabe, M. Tajima, "An algorithm for simulating solid objects suspended in stratified flow," *Comput. Phys. Commun.*, **102**, 147–160 (1997).
17) A. Džiugys, B. J. Peters, "An approach to simulate the motion of spherical and non-spherical fuel particles in combustion chambers," *Granular Matter*, **3**[4], 231–266 (2001).
18) K. F. Malone, B. Xu, "Determination of contact parameters for discrete element method simulations of granular systems," *Particuology*, **6**, 521–528 (2008).
19) K. Morita, T. Matsumoto, R. Akasaka *et al.*, "Development of multicomponent vaporization/condensation model for a reactor safety analysis code SIMMER-III: Theoretical modeling and basic verification," *Nucl. Eng. Des.*, **220**, 224–239 (2003).
20) L. Guo, Y. Kawano, S. Zhang *et al.*, "Numerical simulation of rheological behavior in melting metal using finite volume particle method," *J. Nucl. Sci. Technol.*, **47**[11], 1011–1022 (2010).
21) D. Thomas, "Transport characteristics of suspensions," *J. Colloid Sci.*, **20**, 267–277 (1965).